Persistent Turbulence in the Samoan Passage

JESSE M. CUSACK,[a] GUNNAR VOET,[a] MATTHEW H. ALFORD,[a] JAMES B. GIRTON,[b] GLENN S. CARTER,[c] LARRY J. PRATT,[d] KELLY A. PEARSON-POTTS,[c] AND SHUWEN TAN[d]

[a] *Scripps Institution of Oceanography, University of California, San Diego, La Jolla, California*
[b] *Applied Physics Laboratory, University of Washington, Seattle, Washington*
[c] *University of Hawai'i at Mānoa, Honolulu, Hawaii*
[d] *Woods Hole Oceanographic Institution, Woods Hole, Massachusetts*

(Manuscript received 10 May 2019, in final form 26 September 2019)

ABSTRACT

Abyssal waters forming the lower limb of the global overturning circulation flow through the Samoan Passage and are modified by intense mixing. Thorpe-scale-based estimates of dissipation from moored profilers deployed on top of two sills for 17 months reveal that turbulence is continuously generated in the passage. Overturns were observed in a density band in which the Richardson number was often smaller than $^1/_4$, consistent with shear instability occurring at the upper interface of the fast-flowing bottom water layer. The magnitude of dissipation was found to be stable on long time scales from weeks to months. A second array of 12 moored profilers deployed for a shorter duration but profiling at higher frequency was able to resolve variability in dissipation on time scales from days to hours. At some mooring locations, near-inertial and tidal modulation of the dissipation rate was observed. However, the modulation was not spatially coherent across the passage. The magnitude and vertical structure of dissipation from observations at one of the major sills is compared with an idealized 2D numerical simulation that includes a barotropic tidal forcing. Depth-integrated dissipation rates agree between model and observations to within a factor of 3. The tide has a negligible effect on the mean dissipation. These observations reinforce the notion that the Samoan Passage is an important mixing hot spot in the global ocean where waters are being transformed continuously.

1. Introduction

The Samoan Passage at approximately 170°W, 9°S is a topographic constriction through which around 6 Sv ($1\,\mathrm{Sv} = 10^6\,\mathrm{m^3\,s^{-1}}$) (Rudnick 1997; Voet et al. 2016) of abyssal waters below 4000 m flow from the South Pacific to the North Pacific Ocean basins. It is the largest transport pathway for abyssal waters between these basins, with smaller transports occurring in branches to the east and west (Roemmich et al. 1996). Mixing in the passage drives water mass transformations that show up as sharp along-passage gradients in climatological maps of bottom boundary layer density (Banyte et al. 2018) and potential temperature (Gouretski and Koltermann 2004). Bottom boundary mixing has received significant theoretical attention in recent years as a mechanism for upwelling dense waters and is thought to be an integral component of the global overturning circulation (de Lavergne et al. 2016; Ferrari et al. 2016; McDougall and Ferrari 2017). Mixing in the passage is speculated to be a significant fraction of the total mixing in the North Pacific (Pratt et al. 2019).

Past studies hypothesized that flow acceleration, hydraulic control and mixing were likely to be important processes occurring in the passage (Reid and Lonsdale 1974; Freeland 2001; Roemmich et al. 1996). Recent observations have identified hydraulic jumps and intense turbulence controlled by several bathymetric features, most notably a series of sills, over distances of just a few kilometers (Alford et al. 2013). Most of the volume transport into the passage is contained in a layer of Antarctic Bottom Water and North Atlantic Deep Water (Voet et al. 2015), referred to throughout this paper as the "overflow layer," which is significantly denser than the overlying Pacific Deep Water. The existence of a discernible layer with a sharp density gradient at the interface lends itself to understanding the dynamics using single-layer hydraulic theory

Denotes content that is immediately available upon publication as open access.

Corresponding author: Jesse M. Cusack, jmcusack@ucsd.edu

DOI: 10.1175/JPO-D-19-0116.1

(e.g., Baines 1995), which has been used to successfully describe a hydraulic jump and associated mixing occurring downstream of a major sill in the passage (Thorpe et al. 2018).

Variability in the flow through the passage is caused by tidal forcing, near-inertial waves, and the changes in the low-frequency flow through the passage. Volume transport into the passage below 4000 m ranges from 3 to 8 Sv (Voet et al. 2016). At places in the ocean where tidal flow over topography dominates other lower frequency motions, lee waves and large turbulent overturns can be generated (e.g., Pinkel et al. 2012; Alford et al. 2014; Musgrave et al. 2017). In the Samoan Passage the speed of the overflow layer is typically around 10–20 cm s^{-1} and can exceed 50 cm s^{-1} at sills. Barotropic tidal velocities are about 2 cm s^{-1}, and inertial perturbations can approach 6 cm s^{-1}. Estimates from single-layer theory in a nonrotating, rectangular channel, imply that the layer depth d and overflow velocity v are given by $d \propto Q^{2/3}$ and $v \propto Q^{1/3}$ at the sills, where Q is the volume flux into the channel. Since these power laws are fractional, we expect the flow around the sills to be fairly insensitive to small changes in the volume flux into the passage. It is not clear how rates of turbulent dissipation within the Samoan Passage might change due to these modulations. Observations of a two-layer exchange flow in an abyssal canyon on the flank of the Mid-Atlantic Ridge found an order-of-magnitude increase in the dissipation rate during spring tides (Clément et al. 2017).

Measurements of turbulent dissipation in the ocean are typically confined to single profiles, while few long records exist. The interpretation of such measurements is difficult since turbulence is often intermittent and measurements can be biased by temporal aliasing. Long records allow for the investigation of periodicity in turbulence, which provides information about the physical processes that generate it. The pioneering work of Moum et al. (2013), who created a 6-yr record of turbulence estimates from high-frequency temperature measurements in the equatorial Pacific, found a seasonal cycle in turbulence that was responsible for cooling sea surface temperature. Glider based measurements find that upper ocean turbulence is modulated by wind and buoyancy forcing (Evans et al. 2018). Moored profiler based estimates of turbulent overturns on the Mid-Atlantic Ridge find a correlation between overturn size and the phase of the tide (Clément et al. 2017). These results stand in stark contrast to abyssal observations from near Hawaii, in which one mixing event was observed to dominate a 2.5-yr time series (Alford et al. 2011). Such observations highlight the spatial and temporal variability of abyssal mixing and the need for long-term observations. This paper presents two 500-day time series of overturn-inferred dissipation from moored profilers in the abyss, in which turbulence is found to occur continuously.

The primary goal of this paper is to present observational evidence that mixing in the Samoan Passage is persistent over long times. We argue that topography is the most important factor influencing dissipation rate observed at the moorings. Section 2 outlines the methods and instrumentation. Sections 3a and 3b present a spatial overview of the observations and provide a characterization of mooring observations by their position relative to the sills. In section 3c, long time series of dissipation are presented and analyzed for long-term variability, whereas in section 3d shorter, higher-resolution time series are analyzed for variability at the semidiurnal and inertial period. Section 3e demonstrates that the amount of mixing at the northern sill is consistent with a two-dimensional numerical simulation and that spatial variability explains the majority of variations in mixing between moorings.

2. Method

a. *Moorings*

During the course of the Samoan Passage Abyssal Mixing Experiment (SPAMEX), three mooring arrays were deployed. Their positions are plotted in Fig. 1 with additional details on instrumentation provided in Table 1. A long-term array consisting of seven moorings, labeled M1–M7 and collectively referred to as the M array, was deployed for approximately 17 months (~500 days) between 2012 and 2014. Moorings M1–M4 were deployed at the entrance to the passage to obtain a time series of volume transport (Voet et al. 2016). Moorings M5, M6, and M7 were deployed at the major sills of the passage. They were instrumented with McLane moored profilers (Morrison et al. 2002), which traveled up and down the line, from 20 to 1000 m above bottom at a speed of 25–33 cm s^{-1}, taking about 1 h to conduct a profile. The moored profilers were fitted with Seabird Electronics SBE 52-MP CTDs measuring conductivity, temperature, and pressure and with Falmouth Scientific 2D ACM current meters measuring horizontal currents. The profiler on M7 failed to profile and the current meter on M6 did not collect velocity data. The profilers conducted one profile every 17.4 h, equal to approximately ¼ of the inertial period. Prior to analysis, data from all instruments were averaged into 2-dbar bins.

The short-term moorings, also plotted in Fig. 1, were placed on and around major sills of the passage. The initial short-term array, denoted by the letter P,

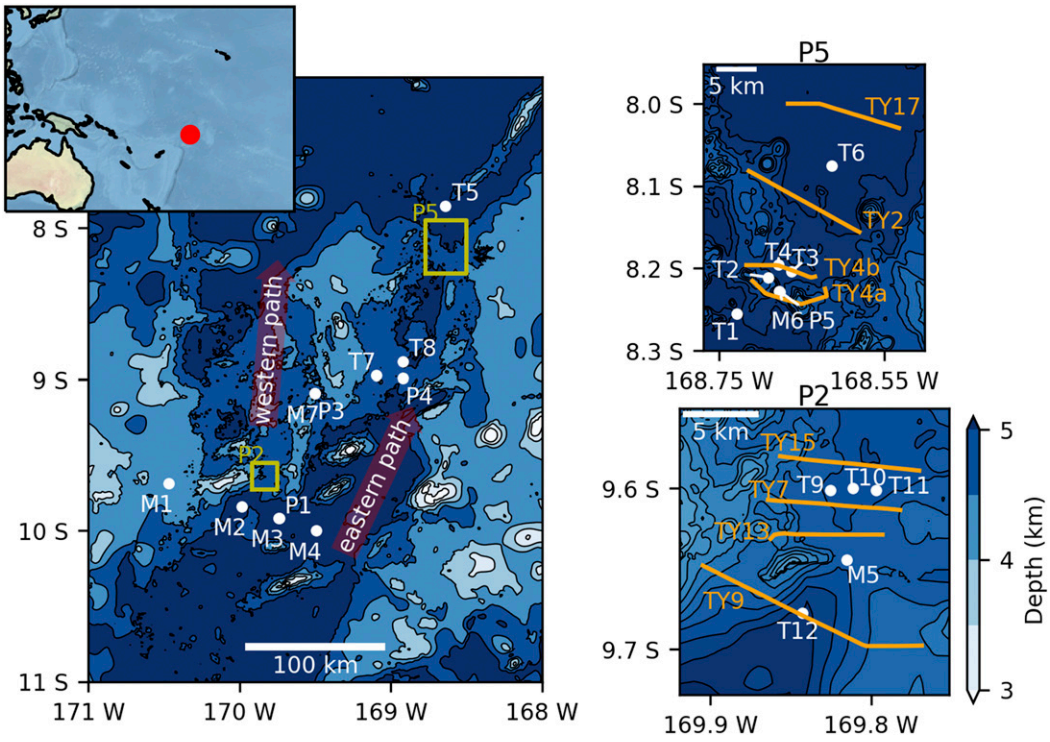

FIG. 1. Overview of the Samoan Passage bathymetry and mooring deployments. The location of the Samoan Passage in the Pacific is shown by the red dot in the inset map. (left) The whole passage, and (expanded from the yellow-outlined areas) sills (bottom right) P2 and (top right) P5, which contain a high concentration of observations. Moorings are denoted by white circles. Tow-yo sections are marked with orange lines. Bathymetry contours are shown at 500-m intervals in the large panel and at 100-m intervals in the smaller panels.

consisted of five moorings each equipped with McLane moored profilers and was deployed in 2012 immediately prior to the M array. The deployment lasted for approximately 3.5 weeks. Most instruments worked as expected with the exception being all instruments on P2 and the current meter on P5. The P5 mooring shares the same location as the M6 mooring. The final short-term array, denoted by the letter T, consisted of 12 moorings

TABLE 1. Mooring record start date and duration, position in longitude and latitude, depth range of moored profiler, and oceanographic parameters recorded by instruments attached to the profiler. The parameters *S*, *T*, *P*, and *V* represent salinity, temperature, pressure, and velocity, respectively.

Mooring	Record start	Duration (days)	Lon	Lat	Depth range (m)	Parameters
P1	24 Jul 2012	24.0	169°44.35′W	9°55.10′S	3540–5198	*S*, *T*, *P*, and *V*
P3	25 Jul 2012	24.7	169°30.21′W	9°5.42′S	3540–4551	*S*, *T*, *P*, and *V*
P4	25 Jul 2012	15.4	168°55.24′W	8°59.57′S	3540–4833	*S*, *T*, *P*, and *V*
P5	26 Jul 2012	26.7	168°40.59′W	8°13.71′S	3540–4895	*S*, *T*, *P*, and *V*
M5	25 Aug 2012	504.6	169°48.92′W	9°38.66′S	3589–4627	*S*, *T*, *P*, and *V*
M6	25 Aug 2012	505.3	168°40.62′W	8°13.67′S	3921–4895	*S*, *T*, and *P*
T1	18 Jan 2014	11.3	168°43.71′W	8°15.32′S	3931–5029	*S*, *T*, *P*, and *V*
T2	17 Jan 2014	2.0	168°41.43′W	8°12.67′S	3931–4753	*S*, *T*, *P*, and *V*
T4	17 Jan 2014	11.0	168°40.68′W	8°11.75′S	3931–4919	*S*, *T*, *P*, and *V*
T5	18 Jan 2014	16.4	168°38.28′W	7°51.23′S	3931–5278	*S*, *T*, *P*, and *V*
T6	23 Jan 2014	10.9	168°36.81′W	8°4.55′S	3935–5113	*S*, *T*, *P*, and *V*
T7	31 Jan 2014	4.8	169°5.73′W	8°58.43′S	3931–4885	*S*, *T*, *P*, and *V*
T8	1 Feb 2014	3.9	168°55.11′W	8°53.03′S	3735–4946	*S*, *T*, *P*, and *V*
T9	6 Feb 2014	6.8	169°49.53′W	9°36.06′S	3544–4683	*S*, *T*, *P*, and *V*
T10	7 Feb 2014	6.7	169°48.69′W	9°35.99′S	3544–4724	*S*, *T*, *P*, and *V*
T11	7 Feb 2014	7.5	169°47.82′W	9°36.08′S	3540–4702	*S*, *T*, *P*, and *V*
T12	7 Feb 2014	6.9	169°50.57′W	9°40.65′S	3344–4889	*S*, *T*, *P*, and *V*

also equipped with moored profilers and was deployed in 2014 immediately after the M array was recovered. The deployments lasted for 1–2 weeks. The profiler on T2 provided only 2 days of full depth data. Similarly, the profiler on T3 did not extend to full depth and produced suspect velocity data. The rest of the T profilers worked as expected. All profilers on the P and T short-term arrays were programmed to profile continuously, with the time between profiles being approximately 25 min and the time to complete a profile being in the range 0.75–1 h, depending on the exact depth range.

b. *Tow-yos*

Tow-yo sections were conducted by raising and lowering the CTD rosette while the ship steamed at approximately 0.7 kt (1 kt $\approx 0.51\,\mathrm{m\,s^{-1}}$). They were taken during January and February 2014 aboard the R/V *Thomas G. Thompson*. The rosette was equipped with upward- and downward-looking 300-kHz RDI acoustic Doppler current profilers (ADCP) and a Seabird Electronics SBE 9 CTD. Horizontal velocities were calculated using the shear-based method (Fischer and Visbeck 1993) and then nudged to bottom-tracking velocities using an inverse method. The lack of shipboard ADCP measurements in the solution, because of upper turnaround depths way beyond the shipboard ADCP reach, leads to higher uncertainty in horizontal velocity higher up in the water column away from the bottom-tracking velocity constraint. The nominal precision of temperature and salinity measurements is $\pm 5 \times 10^{-4}$°C and $\pm 2 \times 10^{-3}$, respectively (Voet et al. 2015). Several of the tow-yos conducted around sills P2 and P5 are shown in Fig. 1. Throughout the text they are given the prefix TY.

c. *Turbulent dissipation from Thorpe scales*

Turbulent kinetic energy dissipation rate, ε, was estimated from turbulent overturning scales using the Thorpe scale method (Thorpe 1977; Dillon 1982). The method relies on observational estimates of the Ozmidov scale L_O, the largest isotropic 3D overturning turbulent scale, and the buoyancy frequency N. Dissipation is then given by

$$\varepsilon = L_O^2 N^3 . \tag{1}$$

The Ozmidov scale is estimated from the Thorpe scale L_T, with $L_O = aL_T$. We use a scaling constant, $a = 0.95$, that is found to produce good agreement with microstructure based estimates of dissipation elsewhere in the Samoan Passage (Voet et al. 2015). The Thorpe scale is calculated as the root-mean-square displacement of water parcels from their statically stable height. Water parcel displacements are detected from unstable patches in profiles of potential density referenced to 4000 dbar, denoted σ_4.

If the density difference between the top and bottom of the patch is not greater than the precision of the density measurement, it is rejected from the analysis. The precision of the potential density measurement is estimated to be $0.001\,\mathrm{kg\,m^{-3}}$ because of random noise in temperature and salinity measurements and then is reduced to $0.0005\,\mathrm{kg\,m^{-3}}$ because of bin averaging with 2-dbar bins and approximately three measurements per dbar. Averaging reduces the resolution of small patches but allows for the detection of larger patches that might be obscured by noise. Pressure is converted to depth using the "TEOS-10" package (IOC et al. 2010) prior to estimating Thorpe scales. The smallest resolvable dissipation rate is approximately $1 \times 10^{-9}\,\mathrm{W\,kg^{-1}}$, roughly equivalent to $L_T = 2.8$ m. The depth-integrated dissipation rate is relatively insensitive to the choice of precision, by less than a factor of 2, which indicates that a small number of easily detected patches contains the majority of the energy. Buoyancy frequency is calculated following Smyth et al. (2001), using the root-mean-square density difference divided by the Thorpe scale to estimate the density gradient. This method is more robust than an average gradient in the case where a patch contains several smaller overturning regions. It also has the additional advantage of being insensitive to errors in determining the patch boundaries. An overturn ratio criterion (Gargett and Garner 2008) of 0.25 is used to reject highly asymmetric patches which are likely to be a result of instrumental error. Where mean dissipation rates are quoted, we refer to the arithmetic mean. The depth-integrated dissipation rate D is calculated as

$$D = \rho_0 \int_{z_0}^{z_1} \varepsilon(z)\, dz , \tag{2}$$

where $\rho_0 = 1000\,\mathrm{kg\,m^{-3}}$ and z denotes depth.

The Thorpe scale method does not directly measure turbulent dissipation scales. It may overestimate the turbulent dissipation rate in locations of gravitational instability and newly formed overturns (Mater et al. 2015). Comparison between dissipation rates estimated from Thorpe scales at the T4 mooring and microstructure based estimates indicates that, at this location, Thorpe scales overestimate dissipation by an order of magnitude (G. S. Carter et al. 2019, unpublished manuscript). Mooring T4 is positioned close to a hydraulic jump where large overturns are newly formed and static instability has been created but the turbulence has not fully developed until farther downstream. However, there is good agreement

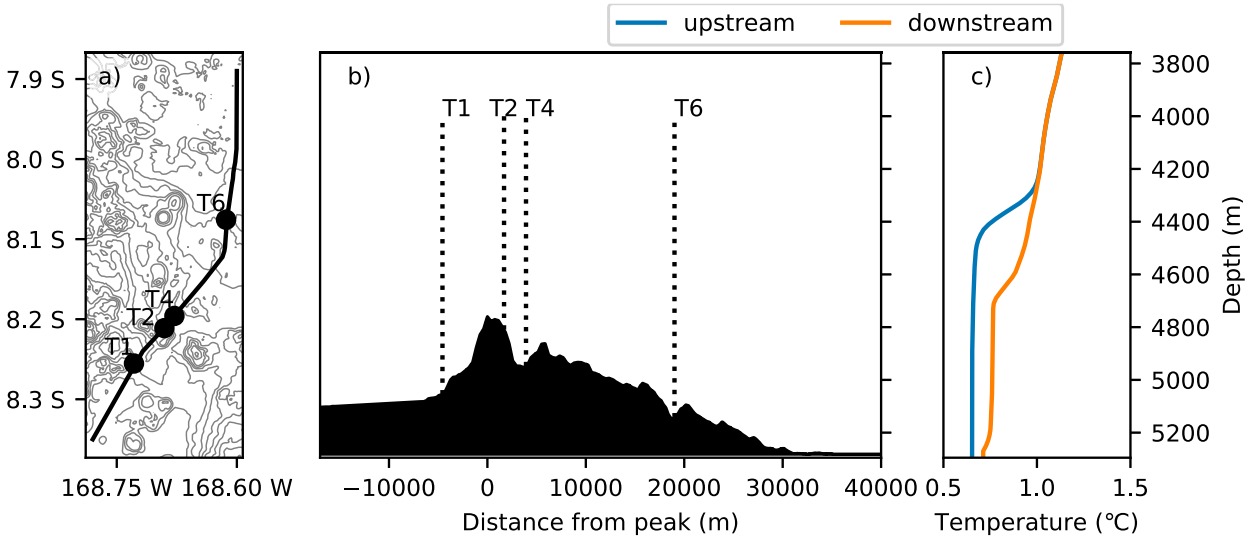

FIG. 2. Overview of the (a) top-down northern (P5) sill bathymetry, contoured in 100-m increments, including the track used for model bathymetry and moorings that fall in the domain, (b) side view of model topography with mooring range marked, and (c) lower portion of upstream and downstream potential temperature profiles used to initialize the model.

between microstructure and Thorpe scales from CTD casts close to the M6 mooring located upstream of the jump. In appendix C of Voet et al. (2015), good agreement is found between spatially averaged Thorpe scales and microstructure dissipation rates for the eastern passage region when using the same scaling constant as used in this paper.

d. Numerical model setup

To investigate questions about spatial and temporal variability in the observations which cannot be easily deduced from point mooring observations n 2D idealized simulation was conducted using a Boussinesq, nonhydrostatic MITgcm configuration (Marshall et al. 1997). Figure 2 shows the model domain and bathymetry, which is based on observations made in 2012 across sill P5. The domain intersects four short-term moorings. The model is initialized using observed upstream and downstream temperature profiles taken from CTD casts, which are displayed in Fig. 2c. Temperature is restored to these profiles in a sponge layer at the domain boundaries. Salinity is kept constant and density is a linear function of temperature only. The two profiles are joined by linear interpolation across the sill to create an along-stream pressure gradient which drives the flow. The resolution is 20 m in both the horizontal and vertical around the sill encompassing a region of 40 km. This is sufficient to resolve the largest overturning scales and tests using the mooring observations find that 90% of the dissipated energy is contained in overturns larger than 20 m. The grid spacing expands linearly either side of this central region such that the total domain length is 565 km and the grid spacing at the boundary is 1000 m. The grid spacing also increases linearly from 20 to 100 m from 4100-m depth to the surface. Topography away from the sill is simplified to be flat or slope at a shallow angle. A barotropic tidal velocity forcing is applied at the domain boundaries with a magnitude of $2\,\mathrm{cm\,s^{-1}}$, consistent with both inverse estimates of the barotropic tide from the region (Egbert and Erofeeva 2002) and those estimated from the mooring observations. A second model run was performed without tidal forcing. Dissipation is parameterized by relating eddy diffusivities and viscosities to density overturning scales in a similar fashion as described above for the observations (Klymak and Legg 2010). The model is run for 12 days and takes 3 days to spin up. The spinup period is removed from the analysis.

3. Results

a. Spatial structure of velocity and dissipation in the Samoan Passage

A detailed analysis of the flow through the Samoan Passage using CTD stations and moorings found that the flow is split into an eastern and western component separated by prominent topography (Voet et al. 2015) as shown in Fig. 1. Subsequent sections of the paper will focus on the more densely observed sills; P2 and P5. Sill P2 is an entrance to the western passage and sill P5 is the northern exit from the eastern passage. Figure 3 displays progressive sections of northward velocity from tow-yo observations at the two sills. The flow speed over P5 is generally greater than at P2.

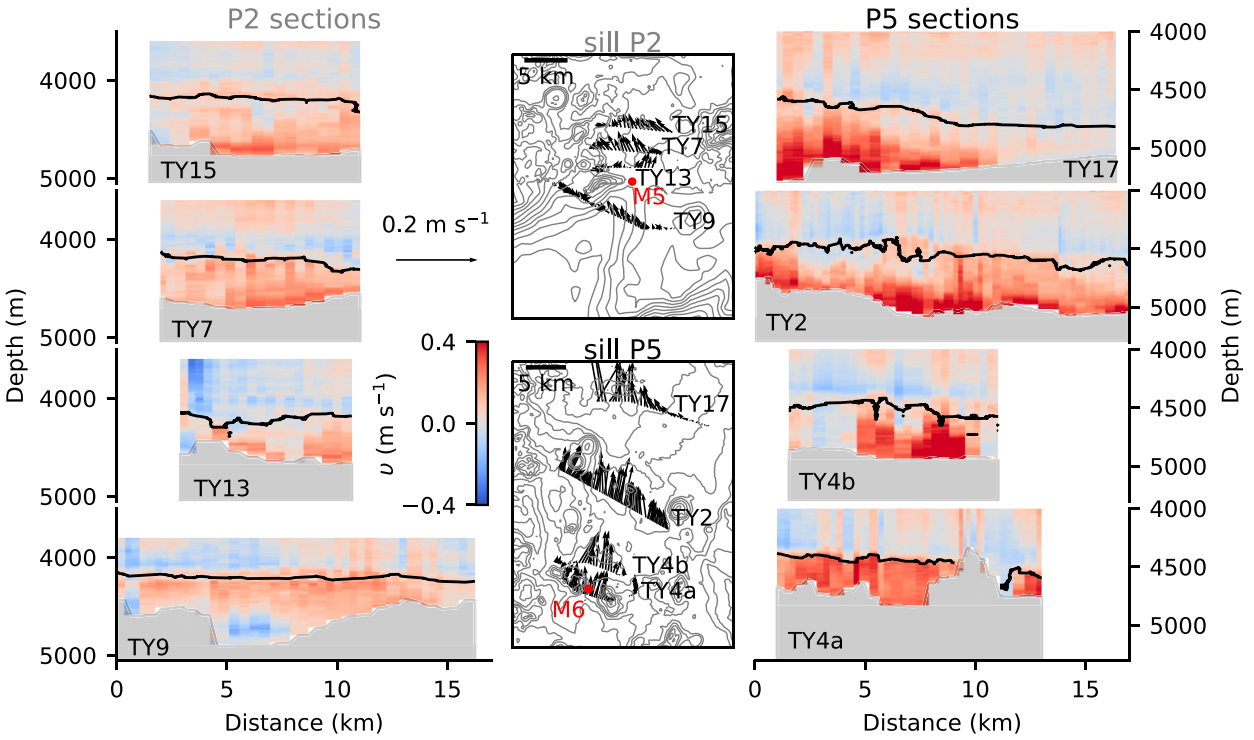

FIG. 3. Tow-yo sections of northward velocity across sills P2 and P5. The sections move progressively from upstream to downstream from the bottom panel to the top panel. Moorings M5 and M6 are marked by a red dot on the maps and correspond to the approximate location of the sill tops. The thin contour in the velocity sections demarks the 45.95 kg m^{-3} isopycnal. The map shows the location of the sections and the depth-averaged velocity vectors within the layer below 45.95 kg m^{-3}. Topography is contoured in 100-m increments.

At both sills the velocity upstream, shown in tow-yo sections TY9 and TY4a, is weaker than downstream. This asymmetry is indicative of hydraulic control which has already been demonstrated at sill P5 and for one side of sill P2 (Alford et al. 2013). The tow-yo sections reveal lateral variability, especially at TY4b (sill P5), which contains a narrow high-velocity jet. This jet is important for interpreting time variability at short-term mooring T4 in a later section. Farther downstream, at TY17 the flow is concentrated on the western side of the channel. The small patch of southward velocity in the deepest portion of TY9 suggests there may be blocking or recirculation of the densest waters approaching sill P2.

b. *A 2D framework for classifying mooring observations*

Figure 3 presents a view of flow over two sills that has both along and across stream structure. We argue here that along-stream variation in the flow has the largest influence on the time mean structure of dissipation at the two sills. We attempt to classify all mooring observations into three dynamical regimes based on idealized theory of flow over a sill. The classification is performed by comparing flow quantities to the theoretical schematic illustrated in Fig. 4. The schematic amalgamates theoretical ideas about stratified flow over sills (Winters and Armi 2014; Jagannathan et al. 2017) and hydraulic jumps (Thorpe et al. 2018), but does not attempt to strictly reproduce the theory. The resulting classification is intentionally qualitative, but provides a useful framework for interpreting the observations. On the left side of the schematic the first regime upstream of the sill is characterized by weak flow and weak dissipation. Some lower portion of the upstream flow may be blocked if it does not have sufficient kinetic energy to mount the sill. In the second regime close to the sill, the flow is fast, and dissipation is concentrated in a shear layer at the interface. A stagnant isolating layer of fluid of low velocity and stratification may be present just above the descending jet. A point of hydraulic control may exist, where the Froude number Fr is equal to 1. The single-layer Fr represents a ratio of the flow speed to the long gravity wave speed and is defined as $\mathrm{Fr} = U/(g'H)^{1/2}$, where g' is the reduced gravity, H is the layer depth, and U is the layer speed. Practically, reduced gravity is estimated as $g\Delta\sigma_4/\overline{\sigma_4}$, where $\Delta\sigma_4$ is the difference in density 100 m above and 100 m below the layer interface and $\overline{\sigma_4}$ is the

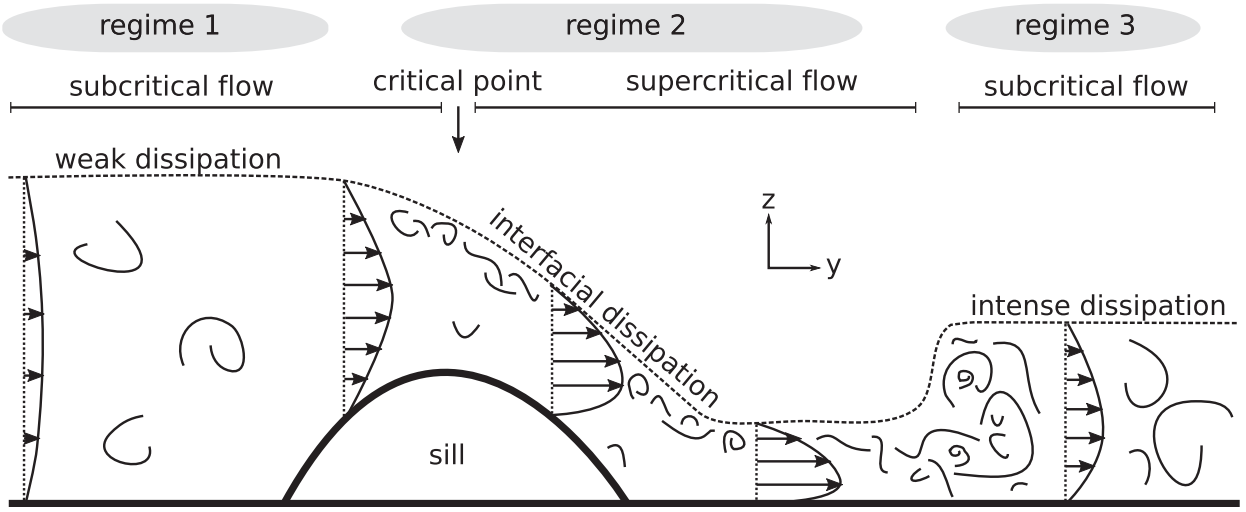

FIG. 4. Idealized 2D representation of flow over a sill. Velocity in the overflow layer is represented by arrows, and turbulence is shown by squiggly lines. In subcritical flow Fr < 1, and in supercritical flow Fr > 1. At the critical point Fr $= 1$.

mean density below the interface. As the flow accelerates over the sill, the upper interface may become susceptible to shear instability. A necessary condition for shear instability is that the gradient Richardson number Ri $< \frac{1}{4}$, where Ri $= N^2/S^2$, with N and S denoting buoyancy frequency and vertical shear respectively (Miles 1961; Howard 1961). In the following analysis shear and buoyancy are calculated over a vertical length scale of 20 m. This supercritical region, where Fr > 1, ends in a turbulent hydraulic jump. The third regime occurs downstream of the sill and hydraulic jump where dissipation is large and encompasses the full depth of the overflow layer. The flow velocity is somewhat slower than at the sill.

The flow regimes characterizing the moorings at sill P5 follow an approximately south-to-north progression across the sill, illustrated by the map in Fig. 5a. Depth-integrated dissipation peaks just downstream of the sill top, at the location of the T4 mooring. The Fr plotted in Fig. 5b as well as the time mean structure of velocity, dissipation, and Ri plotted in Figs. 5c–t, are used to classify moorings into dynamical regimes. Mooring T1 is upstream of the sill and falls into the first regime where the flow velocity and dissipation are relatively weak and Fr is low. A peak in dissipation exists at the layer interface, collocated with a trough in Ri. While Ri is not always observed to be smaller than the critical value, the 10th to 90th percentile range of the distribution denoted by the gray shaded area, does encompass the critical value. At P5, which sits on top of the sill, the layer thickness, defined by the height of the green line, has decreased and dissipation at the interface has intensified. At T2, just downstream of the sill top, the layer thickness has further decreased, Fr is close to critical (Fr $= 0.7$) and dissipation is concentrated at the interface in a region of low Ri associated with strong shear. Moorings P5 and T2 fall into the second regime of interfacial dissipation. Turbulent dissipation at moorings T4 and T6 is very large and peaks below the interface. These moorings are located close to and downstream of the hydraulic jump identified in Alford et al. (2013), where Fr is subcritical, and fall into the intense dissipation regime. Much farther downstream from the jump at T5, the dissipation rate is relatively low, analogous to regime 1.

The flow regimes characterizing the moorings at sill P2 also follow an approximately south-to-north progression across the sill, shown in Fig. 6a. Two moorings, P1 and T12 were located upstream of the sill and exhibit relatively weak flow, weak mixing, and low Fr, placing them in the first dynamical regime. At M5, located close to the sill top, dissipation is concentrated in a several-hundred-meter-thick layer about the interface, corresponding to a local trough in Ri and elevated Fr. However, the Fr is not close to critical at M5 or any of the moorings, suggesting that the flow is not hydraulically controlled at this location. Nevertheless, acceleration of the flow over the sill leads to increased shear and dissipation at the interface suggesting that M5 most closely resembles regime 2. The northern cluster of moorings T9, T10, and T11, located just downstream of the sill top, observe higher dissipation rates than upstream of the sill. For this reason we classify them as falling into the intense mixing regime. However, the dissipation rates are modest when compared with sill

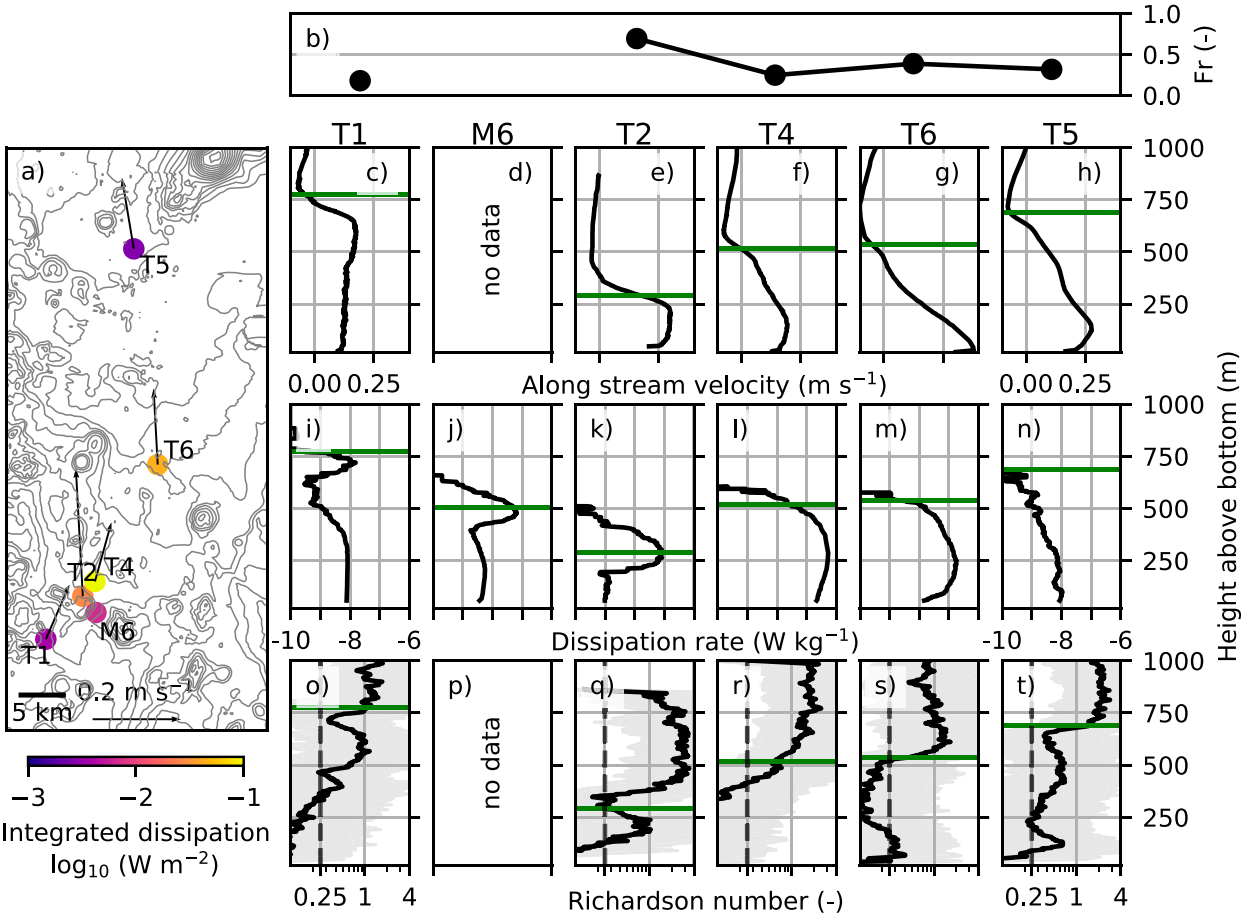

FIG. 5. Time-averaged mooring data from sill P5. (a) Mooring locations in a map colored by depth-integrated dissipation rate. Arrows denote the velocity vector. Bathymetry is contoured at 100-m intervals. (b) Time-mean single-layer Fr at each mooring. (c)–(h) Along-stream velocity at the moorings. Each panel corresponds to the mooring name given at the top. (i)–(n) Dissipation rate. (o)–(t) Ri; the shaded area corresponds to the 10th–90th-percentile range. The vertical dashed line denotes the critical value of 0.25. The horizontal green lines in (c)–(t) denote the interface height estimated from the deepest maxima in buoyancy frequency.

P5. It seems unlikely that a hydraulic jump is the cause of dissipation observed downstream of sill P2.

c. *Long-term dissipation at sills P2 and P5*

Turbulent dissipation in the Samoan Passage is highly persistent. This is illustrated by time series of dissipation from long-term moorings M6 and M5, presented in Figs. 7 and 8. Overturning patches are detected in 62% of profiles at M5 and 97% of profiles at M6. These moorings are located on top of sills P5 and P2 respectively, and fall into the regime of interfacial mixing described previously. At M6, the depth-integrated dissipation rate, plotted in Fig. 7a, has a time mean value of 6.7 (0.5–14.4) $\times$ 10^{-3} W m^{-2}. The values in brackets indicate the 10th–90th-percentile range. Overturns, plotted in Fig. 7c, occur at M6 continuously throughout the time series and are separated into two distinct layers. The upper layer is defined between the two contoured isopycnals σ_4 = (45.93, 45.97) kg m^{-3}, and the lower layer is defined as everything below the lowest contour. Very few overturns were detected in the region above the upper isopycnal, which we neglect from further analysis. Approximately 74% of the dissipation occurs in the upper layer where the dissipation rate averages about (6 $\pm$ 6) $\times$ 10^{-8} W kg^{-1} and occasionally peaks at 4 $\times$ 10^{-6} W kg^{-1}. This layer coincides with a maximum in N^2 which delineates the upper interface of the overflow layer. The interface height can be approximated by the height of the 45.95 kg m^{-3} isopycnal, which has a height standard deviation of 25 m. Strong stratification typically suppresses vertical mixing and this result implies that the shear must be very large, although velocity data are not available to confirm this. Overturns in the lower layer are larger in size but the environment is weakly stratified (Figs. 7d,e) leading to a lower overall dissipation rate.

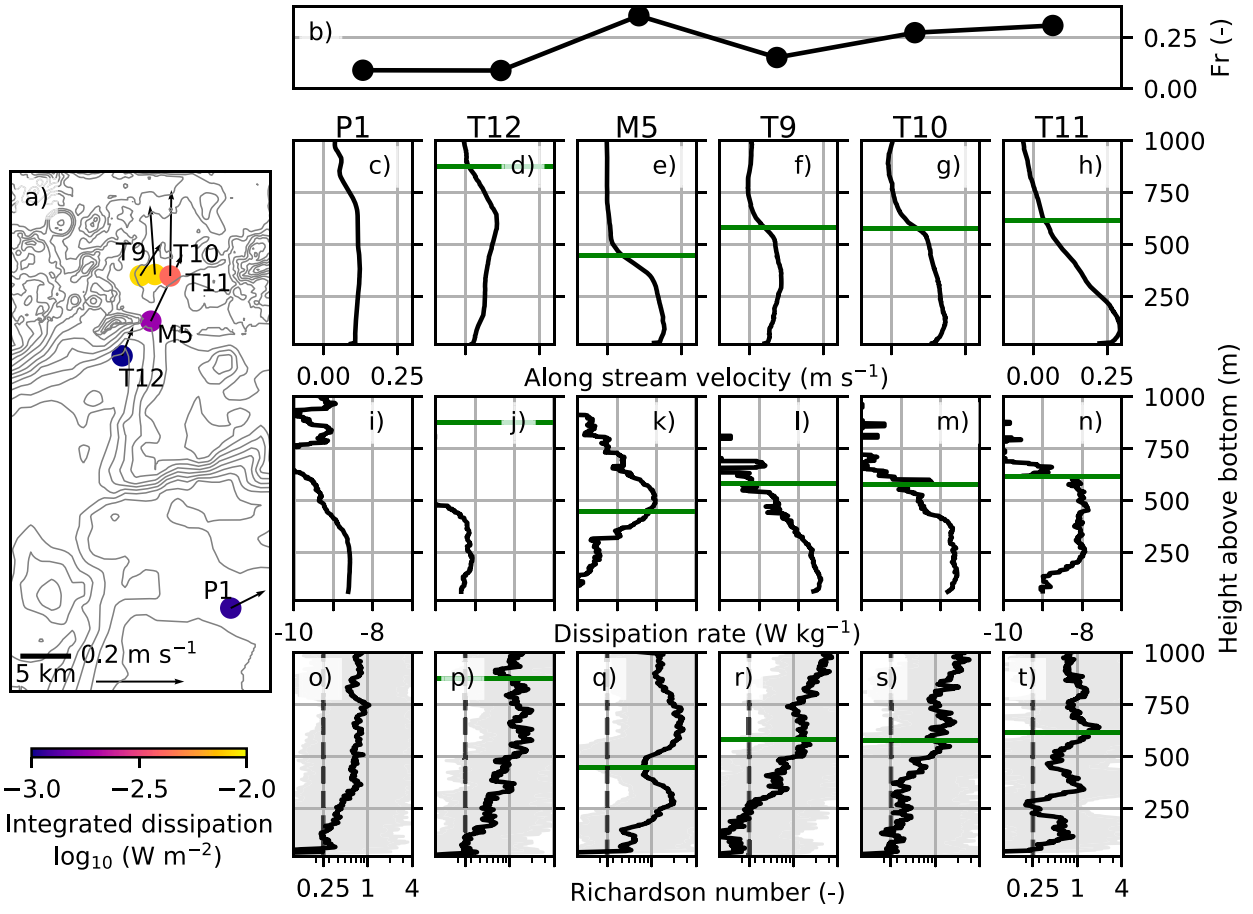

FIG. 6. As in Fig. 5, but from sill P2.

At M5 located at sill P2, overturns occur in a single layer centered at 4160-m depth. The majority of overturns (Fig. 8b) also occur within the isopycnal band $\sigma_4 = (45.93,\ 45.97)\,\mathrm{kg\,m^{-3}}$, corresponding to the "upper layer" at M6. The time-averaged depth-integrated dissipation rate is $1.8\ (0.1\text{–}7.0) \times 10^{-3}\,\mathrm{W\,m^{-2}}$, a factor of 4 smaller than at M6. Along-stream velocity, plotted in Fig. 8e, shows clearly the overflow layer as an ~300-m-thick band of high velocity. Buoyancy frequency (Fig. 8h) exhibits an unusual double peak with the maximum dissipation rate occurring at the local minimum between the two peaks. The interface height can be approximated by the height of the $45.95\,\mathrm{kg\,m^{-3}}$ isopycnal, which has a height standard deviation of 49 m. Velocity observations allow the calculation of shear squared, $S^2 = (\partial u/\partial z)^2 + (\partial v/\partial z)^2$, which is low-pass filtered in depth with a cut off distance of 40 m to remove noise. The filter sets the effective scale over which the shear is calculated, thus the vertical length scale of the shear calculation is also 40 m. Shear is plotted in Fig. 8i and peaks roughly 100 m below the peak in dissipation. The peak in dissipation is within 70 m of a local minimum in Ri, (Figs. 8k,l), which implies that the turbulence is produced by shear instability.

Spectral analysis is performed to assess whether there are any dominant frequencies of variability in the dissipation rate. Spectra of depth-averaged dissipation (Fig. 9a), denoted ϕ_ε, are computed as the average of four 256-point (186 day) half-overlapping time segments, after applying a Hanning window. The data are further frequency-band averaged with a three-point window. These windowing and averaging parameters are chosen pragmatically to reduce noise while maintaining frequency resolution and bandwidth. The final spectrum has 32 effective degrees of freedom (Thomson and Emery 2014). Confidence limits at the 95% level are estimated from the χ^2 probability distribution. Data from M6 have been split into upper and lower layers, corresponding to the isopycnals in Fig. 7c, to investigate whether variability is different between the two layers. The spectra generally appear flat, consistent with a white noise process. The significance of peaks is assessed by testing whether they lie above the 95% confidence limits of a hypothetical white noise

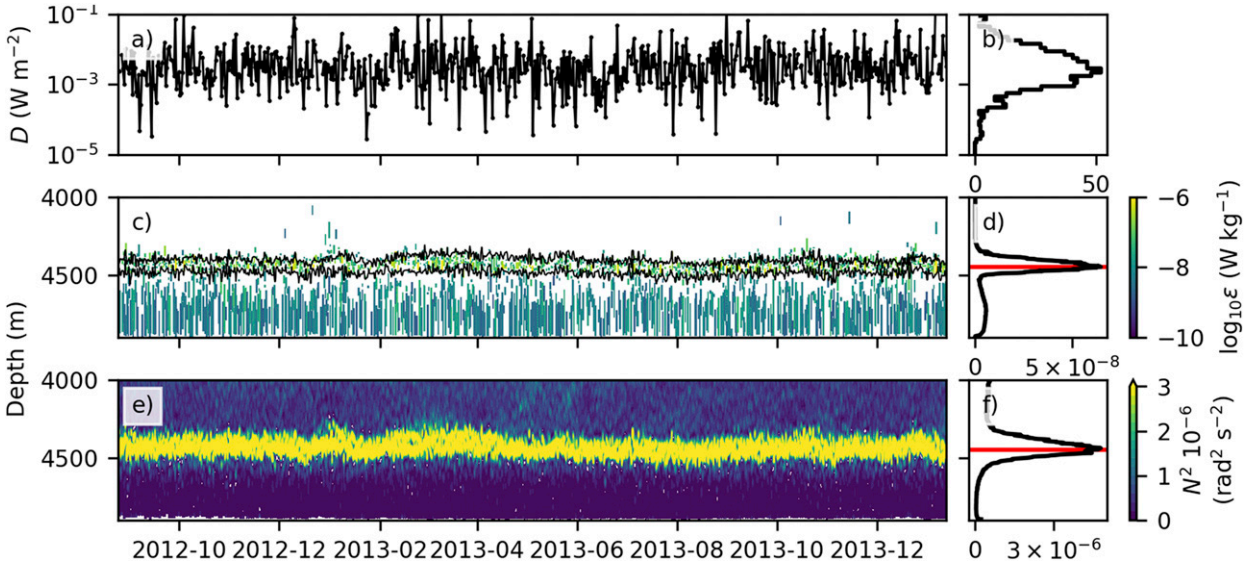

FIG. 7. Time series from mooring M6 of (a) depth-integrated dissipation rate, (c) overturn vertical extent and associated dissipation rate, and (e) buoyancy frequency. (b) Histogram of depth-integrated dissipation. (d),(f) Time averages of (c) and (e), respectively; the horizontal red lines denote the depth of maximum dissipation. The contours in (c) denote the isopycnal depth for $\sigma_4 = (45.93, 45.97)$ kg m^{-3}. An upper layer is defined as the space between the two isopycnals, and a lower layer is defined as the space below the lowest isopycnal. Time is formatted as year-month.

spectrum with the same error as the data. The magnitude of the hypothetical spectrum is taken to be the mean of the data spectrum. There is a significant peak at the M_2 tidal frequency in the spectrum from mooring M5, but no significant peaks in the upper isopycnal level at mooring M6. The peak is consistent with strong semidiurnal variability in velocity observed at M5 (Fig. 9b). The lower level at M6 has significant peaks near the M_2 and Coriolis frequencies. None of the spectra contain significant peaks at time periods greater than a few days, and remain white down to low frequencies.

In the simple case of a single layer, hydraulically controlled channel flow, the dissipation rate occurring in a hydraulic jump (regime 3 in Fig. 4) would be expected to change in response to changes in the upstream volume transport. However, it is unclear how the interfacial dissipation rate (regime 2) will change. We use linear regression analysis to assess whether there is a correlation between flow properties near the sills and the volume transport into the passage measured at moorings M1–M4 (Voet et al. 2016). The speed of the flow over sill P2 is defined as the depth-averaged speed for densities greater than 45.95 kg m^{-3} and further averaged in 3-day bins. It is strongly correlated ($r^2 = 0.64$, where r is the correlation coefficient) with the 3-day-mean volume transport into the passage (Fig. 10a). The correlation between 3-day-averaged depth-integrated dissipation and volume transport (Fig. 10b) is not significant at either M5 ($r^2 < 0.1$) or M6 ($r^2 < 0.1$). These results indicate that the speed of the overflow at the Southern sill is sensitive to changes in volume transport, however, the amount of dissipation occurring at the sill tops appears to be independent of the volume transport.

In December 2012 for a period of 2 weeks the lowest recorded minimum in 100-h low-pass-filtered volume transport was observed, plotted in Fig. 11a. Low-pass filtering was performed to remove tidal variability. The minimum transport was 2.7 Sv, equal to 50% of the record average transport. It was concurrent with a drop of 130 ± 30 m in the interface height at M5, equivalent to 25% ± 5%, which can be most clearly seen in the position of maximum buoyancy frequency plotted in Fig. 11b. This decrease in height is smaller than would be expected from the scaling $d \propto Q^{2/3}$, for which for a 50% drop in the volume flux we expect a 37% drop in the interface height. Departure from conditions of hydraulic control at M5, discussed in section 3b, may limit the relevance of the scaling. A similar drop in interface height was not as pronounced at M6 which is both more distant from the entrance and also located downstream of sill P4 which may complicate the response to mean flow forcing. The depth-integrated dissipation rate (Fig. 11c) averaged over the 2-week period centered on the minimum in volume transport was 1.7 (0.1–3.9) × 10^{-3} W m^{-2} at M5 and 4.9 (0.8–15) × 10^{-3} W m^{-2} at M6. These values are not significantly different from their respective full record averages. This case study provides

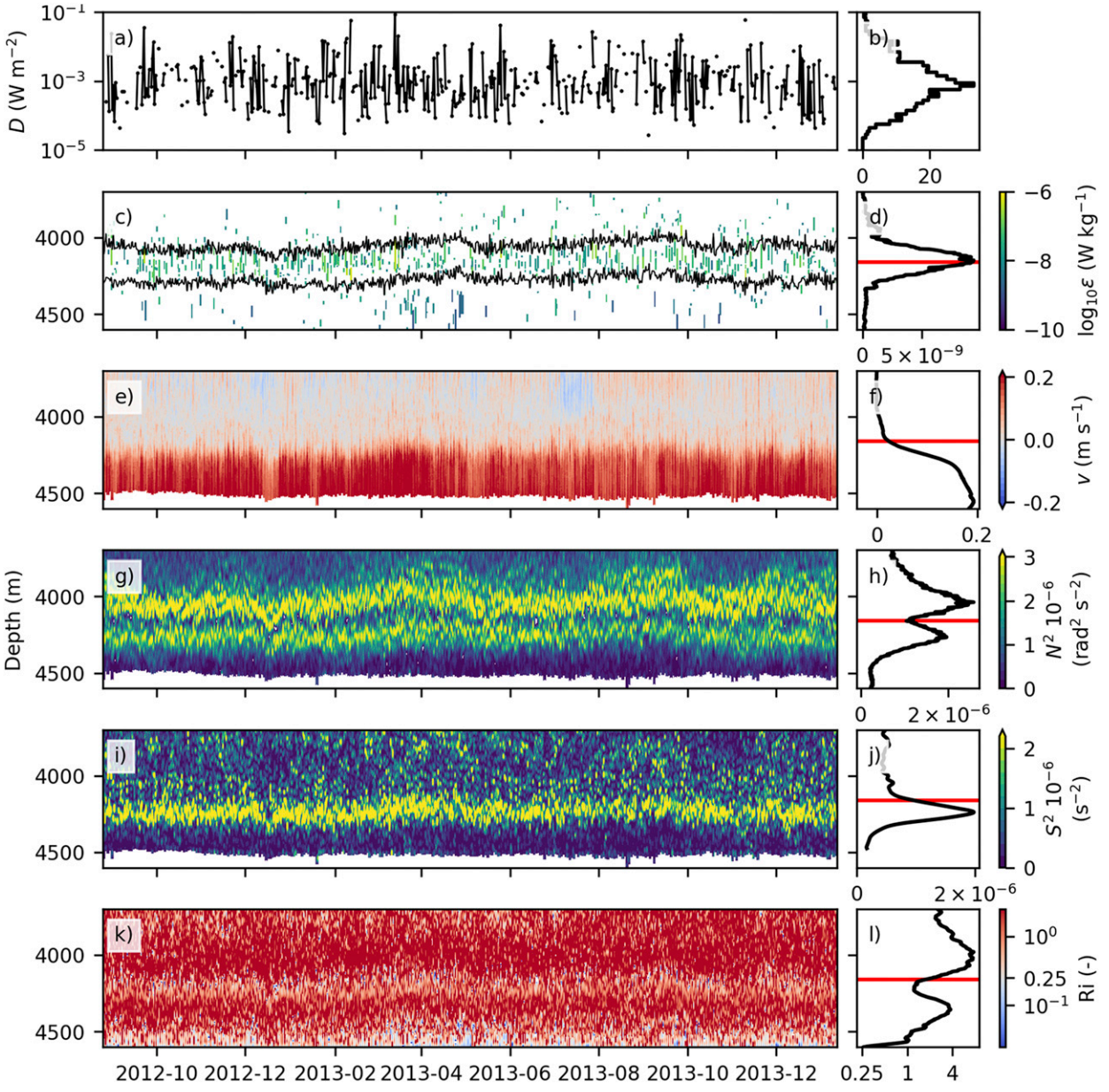

FIG. 8. Time series from mooring M5 of (a) depth-integrated dissipation rate, (c) overturn vertical extent and associated dissipation rate, (e) along-stream velocity, (g) buoyancy frequency, (i) shear squared, and (k) Ri. (b) Histogram of depth-integrated dissipation. (d),(f),(h),(j),(l) Time averages of (c), (e), (g), (i), and (k), respectively; the horizontal red lines denote the depth of maximum dissipation. The contours in (c) denote the isopycnal depth for $\sigma_4 = (45.93, 45.97)$ kg m^{-3}. Time is formatted as year-month.

strong evidence for modulation of flow over sills on time scales greater than a few days, but little evidence that the dissipation rate is affected.

d. *Short-term variability in dissipation*

The sampling frequency and duration of the short-term mooring arrays allow for investigation of variability on time scales from a few hours to a few weeks. Time series of velocity, dissipation and buoyancy frequency are plotted in Fig. 12 for a subsample of moorings. The subsample includes T4, located in a high dissipation environment downstream of a sill, P5 located on top of a sill, T11 located downstream of a sill, and T7 located in the middle of the passage. Tidal variability in along-stream velocity and height of maximum buoyancy frequency are visible in the time series. At all moorings vertical banding indicative of the barotropic and low mode baroclinic tide is superposed

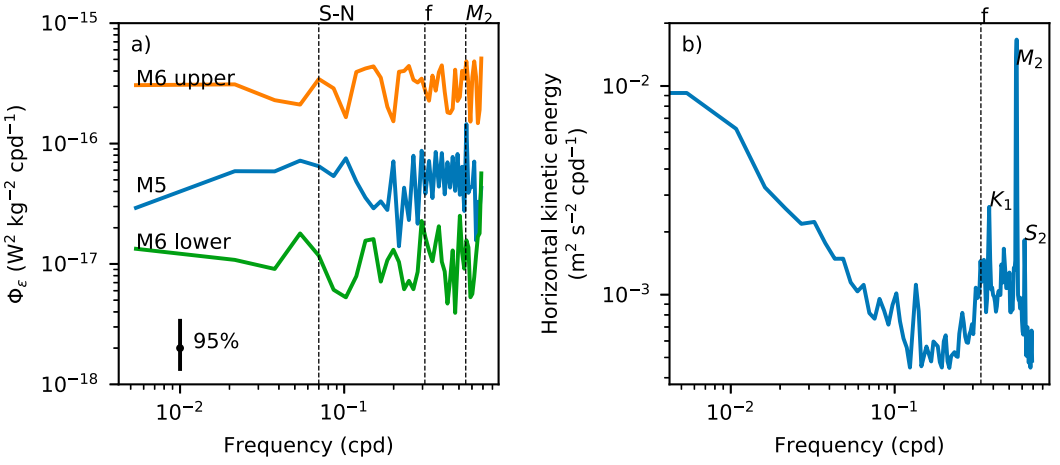

FIG. 9. (a) Spectral variance density of depth-averaged dissipation rate at moorings M5 and M6. Vertical dashed lines denote the position of spring neap (label S–N), Coriolis, and M_2 tidal harmonic frequencies, respectively. The spectra have not been offset. (b) Depth-averaged spectrum of horizontal kinetic energy at M5. Tidal harmonics are labeled and do not appear at their usual frequencies because of aliasing. The vertical line denotes the Coriolis frequency.

on the background flow. At P5 and T4 oscillation of the height of the overflow layer is clear from the position of buoyancy frequency maxima. At T4 the semidiurnal velocity variability in the overflow layer is over 20 cm s^{-1}, much greater than the flow associated with barotropic and baroclinic tides in the abyss. It is likely that meandering of the narrow jet feature in Fig. 3 past the location of the mooring at the semidiurnal period leads to such a large velocity range. A downward-propagating near-inertial wave is visible as diagonal bands in the velocity time series at T11. This wave was also observed at other moorings around sill P2. Dissipation also exhibits near-inertial modulation and is the subject of the subsequent analysis.

Despite significant variability in the overflow speed at tidal or near-inertial frequencies, variability in dissipation is not measurable at most short-term moorings. Consequently, we only present spectral analysis from a subset of moorings which do exhibit notable variability. The spectra are calculated using 32 point windows, which corresponds to between 2.6 and 5 days, depending on the sampling resolution. The depth-averaged Thorpe scale at P1 (Fig. 13a), located near the entrance of the passage, has a small but significant peak close to the M_2 frequency. There is also a large peak in the overflow speed (Fig. 13g), however, dissipation variance does not display a significant peak. Similarly, the Thorpe scale at P4 (Fig. 13b), located in the center of the passage, is modulated at tidal frequencies, but displays no significant peak in dissipation at the same frequency. Dissipation variance at T7 (Fig. 13f) has a significant peak at the M_2 frequency. There is also an increase in dissipation variance toward inertial frequencies. Although the record at T7 is less than 2 inertial periods in length we perform plane wave fits to horizontal velocity. The fits indicate the presence of a near-inertial wave with an amplitude of 1–2 cm s^{-1}. In all cases, the analysis is made difficult by the large-order-of-magnitude range over which dissipation can vary, as well as the short record lengths. These observations hint at an underlying modulation of dissipation at some locations in the passage. However, the modulation is not coherent across the observations, and at most moorings there appears to be little variability in dissipation despite large velocity variability.

The length of the mooring record at M5, which is the only long-term moored profiler record to include velocity data, allows for analysis of variability in the mean flow and mixing at time scales from about 2 days to a year. In the analysis that follows, frequencies of velocity variability are identified and correlated with changes in turbulent dissipation. Dominant frequencies of variability are diagnosed from the depth-averaged spectrum of horizontal kinetic energy which is plotted in Fig. 9b, which contains peaks at the tidal harmonics K_1, M_2, and S_2. Energy is elevated in the internal wave band at frequencies greater than f and also at very low frequencies. The time between profiles at M5 is not small enough to directly resolve tidal components K_1, M_2, and S_2 and causes them to appear as aliased signals with frequencies of 0.38, 0.55, and 0.62 cycles per day (cpd), respectively.

A time series of semidiurnal horizontal kinetic energy on density surfaces is plotted in Fig. 14b. The calculation was performed in density coordinates to remove spurious energy associated with vertical motion of shear maxima.

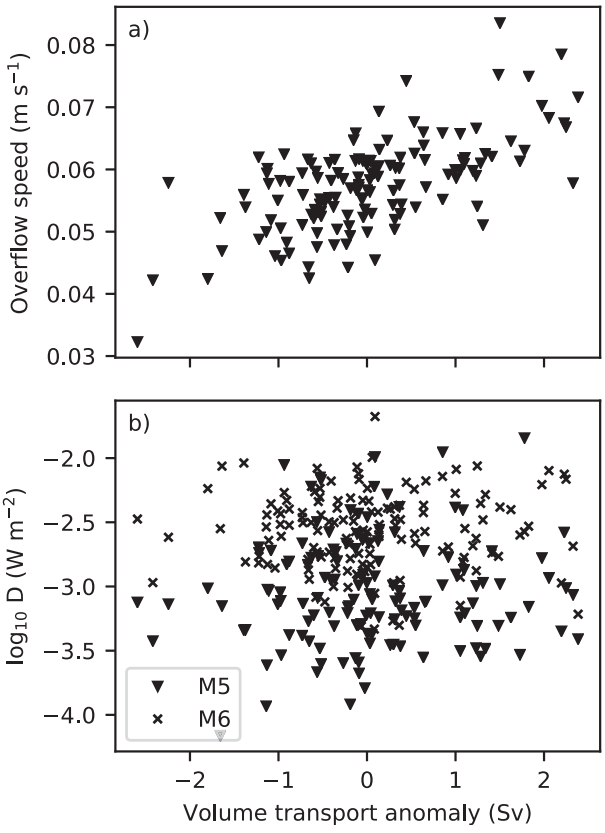

FIG. 10. Three-day-averaged (a) overflow speed at M5 and (b) depth-integrated dissipation rate at M5 and M6, both quantities plotted against volume transport anomaly.

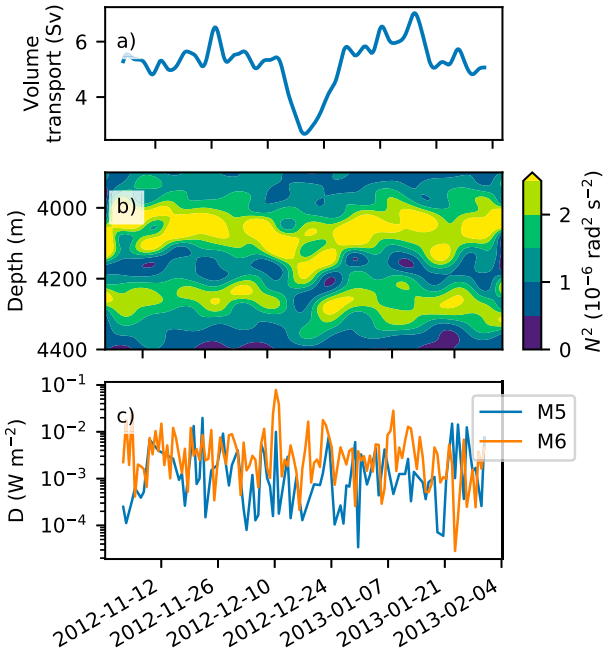

FIG. 11. (a) Volume transport at the entrance of the passage, (b) buoyancy frequency at mooring M5 located at sill P2, and (c) dissipation at M5 and M6.

The velocity in the semidiurnal band was isolated by a fourth-order Butterworth bandpass filter between frequencies 0.45 and 0.65 cpd and the horizontal kinetic energy calculated as $\overline{u_{SD}^2 + v_{SD}^2}$, where the overline denotes a time average over 4 days. The energy is mostly contained in two separate density bands. The upper band, defined as everything above the 45.90 kg m^{-3} isopycnal, is well above the overflow interface and any dissipation. The lower band extends from approximately 45.94 to 45.97 kg m^{-3} and corresponds to the peak in shear. A strongly baroclinic energy structure remains even in density space. The reasons for this are unclear, but may be due to interaction of tides with the rapidly moving overflow layer. Tidal energy occasionally displays spring neap periodicity of 14 days, especially in the upper band, although this signal is intermittent. The spring–neap cycle is caused by interference between tidal constituents M_2 and S_2; however, it is uncertain whether the tidal velocities measured at M5 are generated locally or remotely. The intermittency of the signal suggests that the remote component is significant, since the phase difference between waves can change during their journey.

In Fig. 14a, histograms of turbulent dissipation are compared for time periods when the semidiurnal energy density is greater or less than 0.4 J m^{-3} on the 45.95 kg m^{-3} isopycnal surface. The choice of threshold is arbitrary, but serves the goal of picking out times of higher tidal energy while not being so large as to exclude a significant proportion of the data. The histogram shapes are not sensitive to the choice of threshold, which was varied between 0.3 and 0.5 J m^{-3}, or to the exact choice of bandpass cut off frequency. The shapes of the two histograms are similar, with dissipation rates biased slightly higher when the semidiurnal energy is above the threshold. Periods of higher tidal energy are associated with a factor 1.5 increase in the mean of the distribution, from 2.3×10^{-8} to 3.4×10^{-8} W kg^{-1}. This result may be biased low because the vertical resolution of the data is not sufficient to detect overturns smaller than a few meters. If nonoverturning regions are filled with an assumed background dissipation rate of 6×10^{-11} W kg^{-1} then the factor is 1.8. The number of overturns detected during periods of high near-inertial energy was not sufficient to perform a similar analysis and no significant modulation of dissipation was found at the K_1 frequency.

e. *Modeling of dissipation at sill P5*

Numerical simulations of the northern sill (P5) were run to assess the extent to which observed dissipation

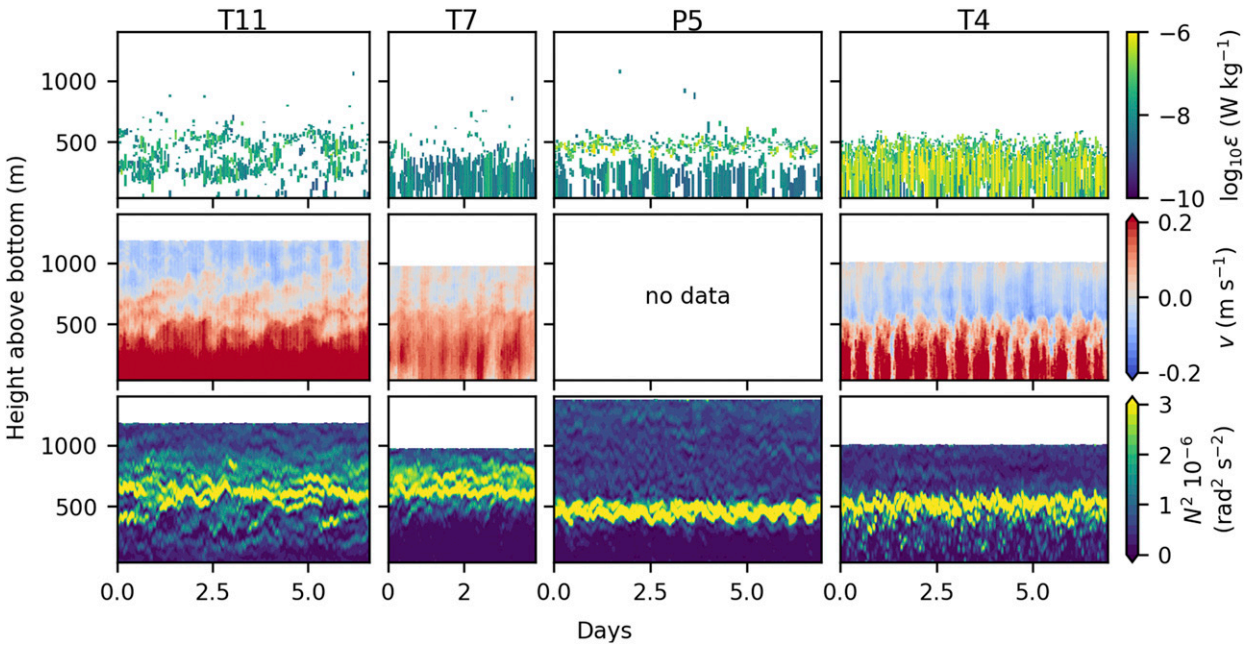

FIG. 12. Time series of (top) turbulent dissipation, (middle) along-stream velocity, and (bottom) buoyancy frequency for moorings (left) T11, (left center) T7, (right center) P5, and (right) T4. The data are not concurrent.

rates are captured by two-dimensional dynamics and whether the addition of a barotropic tide impacts dissipation. This sill was chosen since it contains a high density of along-stream observations with which to compare the model as well as high-resolution bathymetry data. A snapshot of model velocity output is plotted in Fig. 15a. The flow accelerates at the sill and then cascades down the slope. Isothermal surfaces can be seen to plunge on the lee side of the sill. Some surfaces rebound in a hydraulic jump at about 2500 m downstream. Figure 15c compares time-averaged along-stream velocity from moorings T1, T2, T4, and T6 with two numerical model runs, one without tides and the second with a $2\,\mathrm{cm\,s^{-1}}$ barotropic forcing at the M_2 frequency. In the observations, a strong northward flow exists in the bottom layer, the thickness of which can be determined from the height of the zero crossing in northward velocity. This bottom layer flow is northward at all depths deeper than the interface at T1, upstream of the sill, implying that no topographic blocking is taking place. The thickness of the flow decreases and the flow accelerates over the sill at T2 before thickening slightly farther downstream. The numerical model is able to reproduce some of the general features of this overflow, including the lack of upstream blocking, layer thinning and acceleration over the sill as well as the velocity structure at T6 farther downstream. Tidal forcing does not significantly alter the time mean velocity structure in the model, implying the main response of the overflow is a simple addition of the tidal velocity to the preexisting velocity structure that is removed when averaging.

The vertical structure of time-averaged turbulent dissipation upstream of the sill (T1), displayed in Fig. 15d, is much weaker than observed. This can be attributed to the lack of any upstream topography in the model as compared with the real Samoan Passage topography. However, the model does reproduce an intensification in dissipation at the interface of the overflow layer. At the sill top (T2), the thickness of the turbulent layer is thinner in the model than observations and the peak dissipation rate is slightly greater. Downstream dissipation (T4, T6) is of the right order of magnitude but contains mixing at shallower depths not seen in the observations. In the model this is caused by a breaking gravity wave. Depth-integrated dissipation rate in the model, plotted in Fig. 15b, agrees within a factor 2–3 with observations at moorings T2, T4, and T6. The addition of a tidal forcing into the model only marginally changes the depth structure of dissipation and makes almost no difference to the depth-integrated value.

The domain average dissipation rate (Fig. 16) asymptotes to a value of $\sim 4 \times 10^{-8}\,\mathrm{W\,kg^{-1}}$ after about 3 days, the time in the model required to spin up a steady flow over the sill. There is no significant difference in the magnitude or time dependence of the dissipation rate between the tide and no tide simulations. The average is only calculated over the region where the model resolution is 20 m, between −6.6 and 33.3 km. Although the bathymetry of the northern sill contains complex three-dimensional

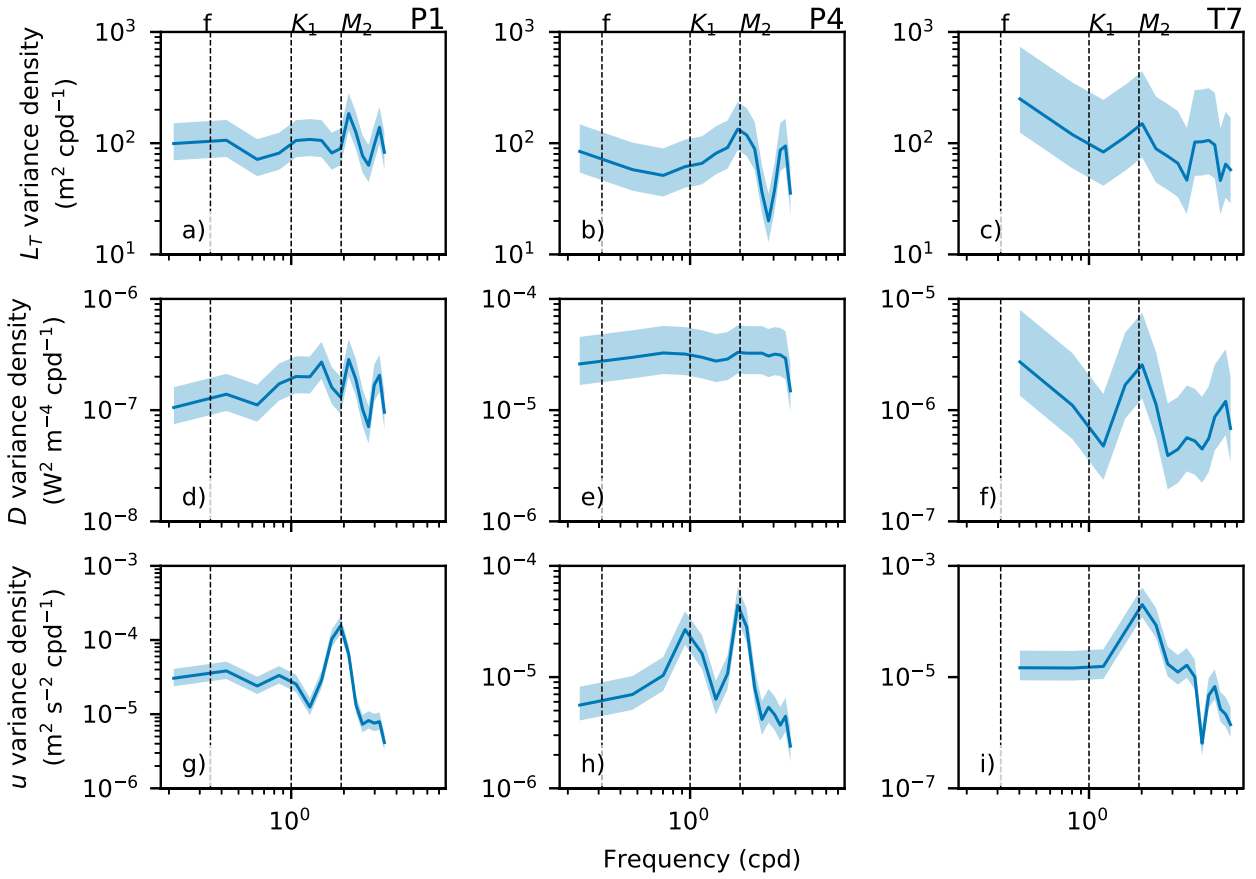

FIG. 13. Variance spectral density of (a)–(c) depth-averaged Thorpe scale, (d)–(f) depth-integrated dissipation, and (g)–(i) overflow average velocity for moorings (left) P1, (center) P4, and (right) T7. The shaded region denotes the 95% confidence interval. The vertical dashed lines denote the Coriolis frequency and K_1 and M_2 tidal constituents.

structure not captured by this model, the time-averaged properties of the flow are generally consistent with a two dimensional formulation of the dynamics.

4. Discussion and conclusions

Data from moorings in the Samoan Passage were analyzed to generate time series of turbulent dissipation. The dissipation was found to occur primarily within, and at the interface of, a dense bottom water layer that flows northward through the passage. Two long time series reveal that turbulence previously identified to be occurring around two sills within the passage is generated continuously. The location of the long-term moorings on top of sills is such that they sampled turbulence generated as a result of shear instability at

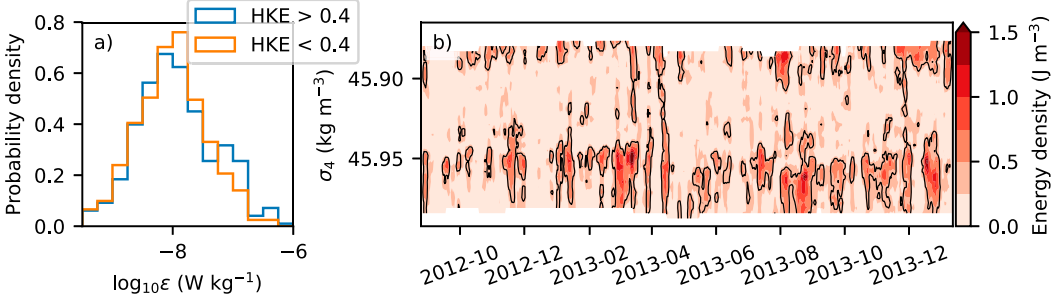

FIG. 14. (a) Probability distribution of dissipation at times when the horizontal kinetic energy (label HKE) density in the semidiurnal band exceeds the threshold value of 0.4 J m^{-3}. (b) HKE density in the semidiurnal band at M5 in density coordinates. A thin black contour delineates regions where the energy exceeds the threshold.

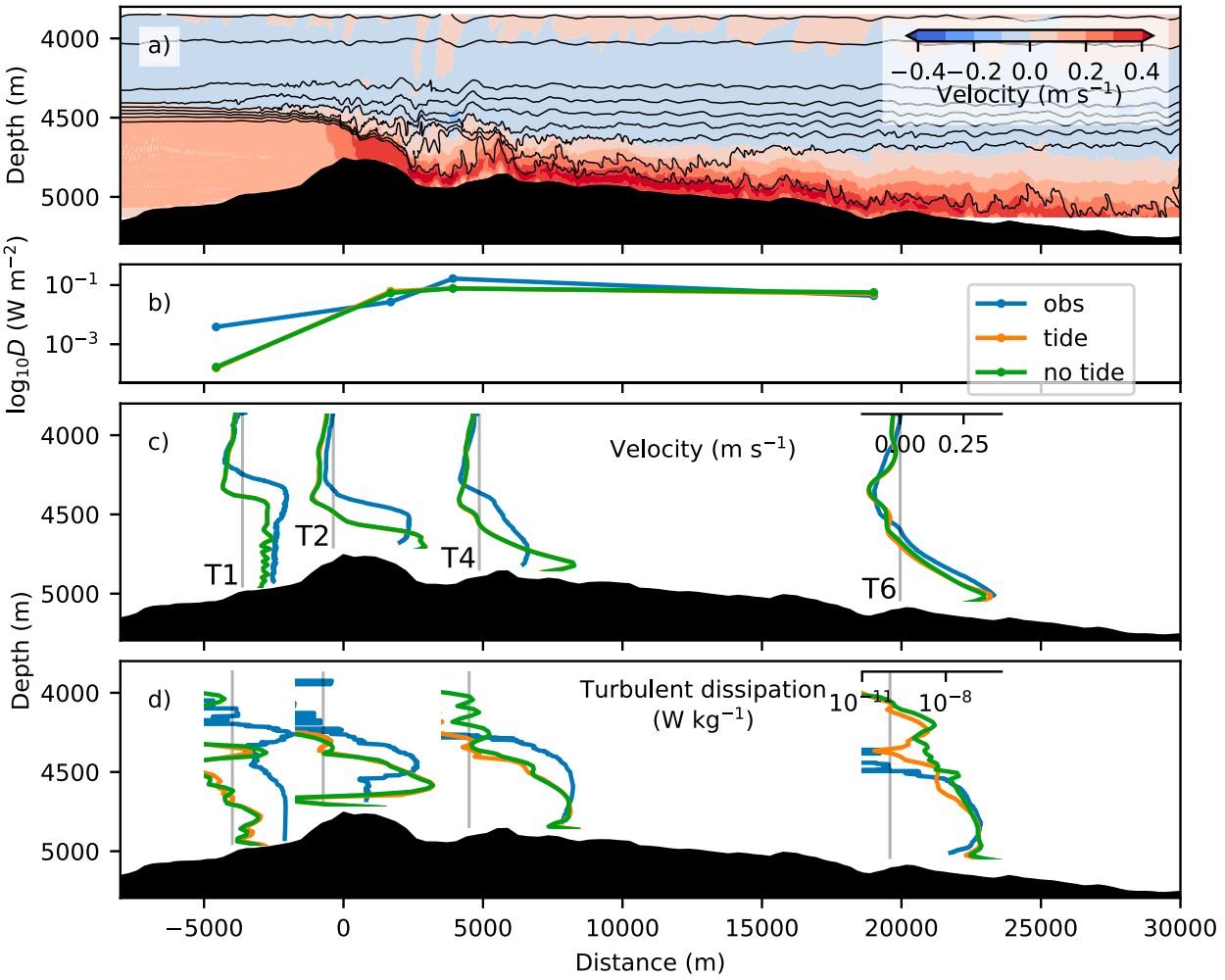

FIG. 15. (a) A snapshot of northward velocity from the numerical model that includes tidal forcing. Isotherms are contoured in 0.05°C increments. Quantities compared between model and observations: (b) depth-integrated dissipation, (c) time-averaged along-stream velocity, and (d) time-averaged dissipation rate. The barotropic tidal forcing in the model was 2 cm s^{-1}.

the overflow interface. Short-term moorings situated upstream and downstream of sills show a transition from weak interior dissipation to intense downstream dissipation. The magnitude and vertical structure of dissipation and velocity at the moorings can largely be explained by their location relative to sills and a hydraulic jump.

A 2-week period when the volume flux into the passage dropped by 50% was correlated with a drop in the overflow interface height, but had no impact on the dissipation rate at either the Northern or Southern sill. No correlation was found between volume flux into the passage and dissipation occurring on top of the two sills. We conclude that conditions at sills in the passage are always conducive to shear instability, even at times of lower than average flow. This contrasts to other regions of the abyssal ocean where turbulent events can be highly intermittent (Alford et al. 2011).

While long-term observations were confined to sill tops, it is possible to speculate on the sensitivity of downstream dissipation in a hydraulic jump to changes in upstream conditions. Thorpe et al. (2018) provide a simple parameterization for the dissipation rate of a hydraulic jump in a continuously stratified shear layer [their Eq. (3.1)]. It depends on the change in thickness of the shear layer across the jump and the prejump overflow speed U^3. Assuming hydraulic control at a sill upstream of the jump leads to a linear dependence on the volume flux Q. Single-layer, nonrotating theory provides the result that $\varepsilon \propto Q[(d_d - d_u)^3/(d_u d_d)]$, where d_u and d_d are the layer depth upstream and downstream of the jump (Pratt and Whitehead 2007). These two formulations of the theory have a linear dependence

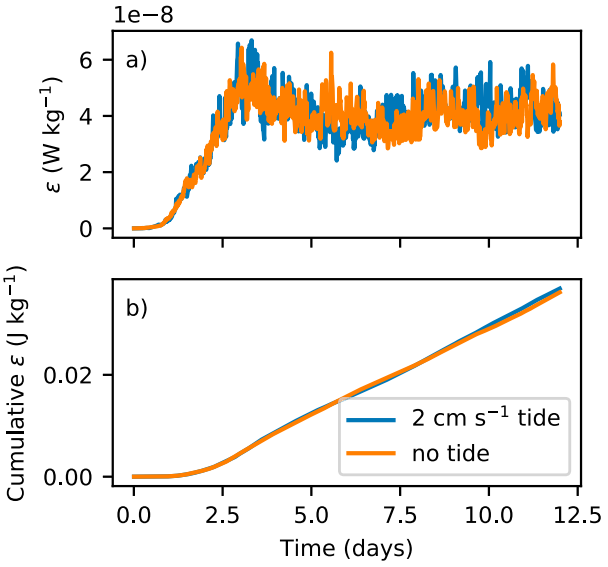

FIG. 16. Estimates of (a) domain average dissipation with and without tides and (b) cumulative dissipation from the numerical model.

of the dissipation rate on the volume flux. Importantly, they also have a dependence on layer depths on either side of the jump. Hydraulic control theory generally dictates that if Q decreases, the layer depth at the sill crest will decrease, the position of the hydraulic jump will shift closer to the sill, and $d_d - d_u$ will decrease. (If Q is decreased enough, the hydraulic control and jump will be lost and $d_d - d_u$ will vanish.) The expectation, therefore, is that the factor $(d_d - d_u)^3/(d_u d_d)$ will decrease as Q decreases. Further numerical simulations of flow over sills with realistic topography would be required to provide a better assessment.

Observations from some short-term moorings capture tidal and near-inertial variability in both velocity and dissipation. The uncertainty in Thorpe scale estimates as well as the inherently noisy nature of turbulence make it difficult to draw confident conclusions as to the significance of these modulations. The mean dissipation rate at a Southern Sill does increase by a factor of 1.5 in time periods when the tidal energy is larger. This is associated with a small positive shift in the probability distribution of the turbulent dissipation rate at times of higher tidal energy. Tidal variability of dissipation in the passage is much smaller than that seen on the flank of the Mid-Atlantic Ridge (Clément et al. 2017). Turbulence in the passage appears to be always present, in contrast to some regions of the ocean, such as Kaena Ridge, where mixing is much greater at one phase of the tide (Alford et al. 2014). A numerical model of the northern sill without tides or any other high-frequency forcing is able to capture time mean magnitude and structure of dissipation at the northern sill to within a factor of 2–3.

Recent research has suggested conditions of hydraulic control in an Arctic channel exist even when the tidal velocity perturbation is larger than the overflow speed (Hughes et al. 2018). The authors attribute this stability to the long time scale necessary to alter hydraulic conditions, which require upstream conditions to equilibrate and a lee wave to form. The time scales for these are greater than the tidal period. In the Samoan Passage, where the overflow velocity exceeds tidal and near-inertial perturbations, it follows that the hydraulic conditions are not strongly affected. Helfrich (1995) provides a parameter relevant to assessing the significance of temporal forcing on a two layer hydraulic flow. While the flow through the passage is more analogous to a single-layer flow, the parameter should also apply here. It is a ratio of the forcing velocity u_F to the flow speed at a sill $(g'H)^{1/2}$. We find that the ratio of these quantities is less than 0.1 at all mooring locations when using $u_F = 2\,\mathrm{cm\,s^{-1}}$. The tidal velocity amplitude would need to be $\sim 10\,\mathrm{cm\,s^{-1}}$ to significantly alter the flow. We do not rule out the possibility that some regions of the passage may be more susceptible to tidal forcing caused by internal tides propagating from remote locations, local internal tide generation or a local resonant response. The mooring data include several downward-propagating near-inertial waves with a velocity amplitude much larger than the barotropic tide (Pearson-Potts 2019). These may have a greater effect on the local flow. Nevertheless, Voet et al. (2015) argue that the majority of mixing taking place in the passage is at hotspots downstream of hydraulically controlled sills and as such we would expect the Samoan Passage average dissipation rate to be insensitive to high-frequency perturbations.

Conditions of hydraulic control have been identified in other regions of dense abyssal overflows, such as Denmark Strait (Käse and Oschlies 2000) and Faroe Bank Channel (Girton et al. 2006). It is possible that similar insensitivity in mixing to high-frequency perturbations is also present at these locations. The persistence of dissipation in the Samoan Passage is relevant to a recent estimate (Pratt et al. 2019) of the northward transport that avoids the Samoan Passage and is instead diverted around the eastern side of the Manihiki Plateau. The estimate, which is based on an abyssal and steady-state form of the island rule (Godfrey 1989), requires the total rate of energy dissipation in the Samoan Passage is constant in time. The results presented in this paper provide confidence that values of dissipation rate previously reported (Alford et al. 2013; Voet et al. 2015), as well as a geography of microstructure observations for the whole passage (Carter et al. 2019), are likely to

be representative of the time mean conditions in the Samoan Passage.

Acknowledgments. The authors thank Zhongxiang Xao and Jody Klymak, who provided earlier setups of the numerical model, and also Arjun Jagannathan for insightful discussions on the subject of flow over topography. We also thank John Mickett and Eric Boget for their assistance in designing, deploying, and recovering the moorings. In addition, we also thank the crew and scientists aboard the R/V *Revelle* and R/V *Thompson*, without whom the data presented in this paper could not have been gathered. Ilker Fer and two anonymous reviewers provided thoughtful feedback that improved the paper. This work was supported by the National Science Foundation under Grants OCE-1029268, OCE-1029483, OCE-1657264, OCE-1657795, OCE-1657870, and OCE-1658027.

REFERENCES

Alford, M. H., R. Lukas, B. Howe, A. Pickering, and F. Santiago-Mandujano, 2011: Moored observations of episodic abyssal flow and mixing at station ALOHA. *Geophys. Res. Lett.*, **38**, L15606, https://doi.org/10.1029/2011GL048075.

——, J. B. Girton, G. Voet, G. S. Carter, J. B. Mickett, and J. M. Klymak, 2013: Turbulent mixing and hydraulic control of abyssal water in the Samoan Passage. *Geophys. Res. Lett.*, **40**, 4668–4674, https://doi.org/10.1002/grl.50684.

——, J. M. Klymak, and G. S. Carter, 2014: Breaking internal lee waves at Kaena Ridge, Hawaii. *Geophys. Res. Lett.*, **41**, 906–912, https://doi.org/10.1002/2013GL059070.

Baines, P. G., 1995: The flow of a homogeneous layer with a free surface. *Topographic Effects in Stratified Flows*, Cambridge University Press, 17–92.

Banyte, D., D. A. Smeed, and M. Morales Maqueda, 2018: The weakly stratified bottom boundary layer of the global ocean. *J. Geophys. Res. Oceans*, **123**, 5587–5598, https://doi.org/10.1029/2018JC013754.

Carter, G. S., and Coauthors, 2019: A spatial geography of abyssal turbulent mixing in the Samoan Passage. *Oceanography*, in press.

Clément, L., A. M. Thurnherr, and L. C. St. Laurent, 2017: Turbulent mixing in a deep fracture zone on the Mid-Atlantic Ridge. *J. Phys. Oceanogr.*, **47**, 1873–1896, https://doi.org/10.1175/JPO-D-16-0264.1.

de Lavergne, C., G. Madec, J. Le Sommer, A. J. G. Nurser, and A. C. Naveira Garabato, 2016: The impact of a variable mixing efficiency on the abyssal overturning. *J. Phys. Oceanogr.*, **46**, 663–681, https://doi.org/10.1175/JPO-D-14-0259.1.

Dillon, T. M., 1982: Vertical overturns: A comparison of Thorpe and Ozmidov length scales. *J. Geophys. Res.*, **87**, 9601–9613, https://doi.org/10.1029/JC087iC12p09601.

Egbert, G. D., and S. Y. Erofeeva, 2002: Efficient inverse modeling of barotropic ocean tides. *J. Atmos. Oceanic Technol.*, **19**, 183–204, https://doi.org/10.1175/1520-0426(2002)019<0183:EIMOBO>2.0.CO;2.

Evans, D. G., and Coauthors, 2018: Annual cycle of turbulent dissipation estimated from Seagliders. *Geophys. Res. Lett.*, **45**, 10 560–10 569, https://doi.org/10.1029/2018GL079966.

Ferrari, R., A. Mashayek, T. J. McDougall, M. Nikurashin, and J.-M. Campin, 2016: Turning ocean mixing upside down. *J. Phys. Oceanogr.*, **46**, 2239–2261, https://doi.org/10.1175/JPO-D-15-0244.1.

Fischer, J., and M. Visbeck, 1993: Deep velocity profiling with self-contained ADCPs. *J. Atmos. Oceanic Technol.*, **10**, 764–773, https://doi.org/10.1175/1520-0426(1993)010<0764:DVPWSC>2.0.CO;2.

Freeland, H., 2001: Observations of the flow of abyssal water through the Samoa Passage. *J. Phys. Oceanogr.*, **31**, 2273–2279, https://doi.org/10.1175/1520-0485(2001)031<2273:OOTFOA>2.0.CO;2.

Gargett, A., and T. Garner, 2008: Determining Thorpe scales from ship-lowered CTD density profiles. *J. Atmos. Oceanic Technol.*, **25**, 1657–1670, https://doi.org/10.1175/2008JTECHO541.1.

Girton, J. B., L. J. Pratt, D. A. Sutherland, and J. F. Price, 2006: Is the Faroe Bank Channel overflow hydraulically controlled? *J. Phys. Oceanogr.*, **36**, 2340–2349, https://doi.org/10.1175/JPO2969.1.

Godfrey, J. S., 1989: A Sverdrup model of the depth-integrated flow for the world ocean allowing for island circulations. *Geophys. Astrophys. Fluid Dyn.*, **45**, 89–112, https://doi.org/10.1080/03091928908208894.

Gouretski, V., and K. P. Koltermann, 2004: WOCE global hydrographic climatology. Berichte des Bundesamtes für Seeschifffahrt und Hydrographie 35, 52 pp.

Helfrich, K. R., 1995: Time-dependent two-layer hydraulic exchange flows. *J. Phys. Oceanogr.*, **25**, 359–373, https://doi.org/10.1175/1520-0485(1995)025<0359:TDTLHE>2.0.CO;2.

Howard, L. N., 1961: Note on a paper of John W. Miles. *J. Fluid Mech.*, **10**, 509, https://doi.org/10.1017/S0022112061000317.

Hughes, K. G., J. M. Klymak, W. J. Williams, and H. Melling, 2018: Tidally modulated internal hydraulic flow and energetics in the central Canadian Arctic Archipelago. *J. Geophys. Res. Oceans*, **123**, 5210–5229, https://doi.org/10.1029/2018JC013770.

IOC, SCOR, and IAPSO, 2010: The international thermodynamic equation of seawater—2010: Calculation and use of thermodynamic properties. UNESCO Intergovernmental Oceanographic Commission Manuals and Guides 56, 196 pp., http://www.teos-10.org/pubs/TEOS-10_Manual.pdf.

Jagannathan, A., K. B. Winters, and L. Armi, 2017: Stability of stratified downslope flows with an overlying stagnant isolating layer. *J. Fluid Mech.*, **810**, 392–411, https://doi.org/10.1017/jfm.2016.683.

Käse, R. H., and A. Oschlies, 2000: Flow through Denmark Strait. *J. Geophys. Res.*, **105**, 28 527–28 546, https://doi.org/10.1029/2000JC900111.

Klymak, J. M., and S. M. Legg, 2010: A simple mixing scheme for models that resolve breaking internal waves. *Ocean Modell.*, **33**, 224–234, https://doi.org/10.1016/j.ocemod.2010.02.005.

Marshall, J., A. Adcroft, C. Hill, L. Perelman, and C. Heisey, 1997: A finite-volume, incompressible Navier Stokes model for studies of the ocean on parallel computers. *J. Geophys. Res.*, **102**, 5753–5766, https://doi.org/10.1029/96JC02775.

Mater, B. D., S. K. Venayagamoorthy, L. St. Laurent, and J. N. Moum, 2015: Biases in Thorpe-scale estimates of turbulence dissipation. Part I: Assessments from large-scale overturns in oceanographic data. *J. Phys. Oceanogr.*, **45**, 2497–2521, https://doi.org/10.1175/JPO-D-14-0128.1.

McDougall, T. J., and R. Ferrari, 2017: Abyssal upwelling and downwelling driven by near-boundary mixing. *J. Phys. Oceanogr.*, **47**, 261–283, https://doi.org/10.1175/JPO-D-16-0082.1.

Miles, J. W., 1961: On the stability of heterogeneous shear flows. *J. Fluid Mech.*, **10**, 496, https://doi.org/10.1017/S0022112061000305.

Morrison, A., J. Billings, and K. Doherty, 2002: The McLane moored profiler: an autonomous platform for oceanographic measurements. *OCEANS 2000 MTS/IEEE Conf. and Exhibition*, Providence, RI, IEEE, 353–358, https://doi.org/10.1109/OCEANS.2000.881284.

Moum, J. N., A. Perlin, J. D. Nash, and M. J. McPhaden, 2013: Seasonal sea surface cooling in the equatorial Pacific cold tongue controlled by ocean mixing. *Nature*, **500**, 64–67, https://doi.org/10.1038/nature12363.

Musgrave, R. C., J. A. MacKinnon, R. Pinkel, A. F. Waterhouse, J. Nash, and S. M. Kelly, 2017: The influence of subinertial internal tides on near-topographic turbulence at the Mendocino Ridge: Observations and modeling. *J. Phys. Oceanogr.*, **47**, 2139–2154, https://doi.org/10.1175/JPO-D-16-0278.1.

Pearson-Potts, K., 2019: Deep near-inertial waves in the Samoan Passage. Ph.D. dissertation, University of Hawai'i at Mānoa, 140 pp.

Pinkel, R., M. Buijsman, and J. Klymak, 2012: Breaking topographic lee waves in a tidal channel in Luzon Strait. *Oceanography*, **25** (2), 160–165, https://doi.org/10.5670/oceanog.2012.51.

Pratt, L. J., and J. A. Whitehead, 2007: Review of the Hydraulics of Nonrotating, Homogeneous Flow. *Rotating Hydraulics, Springer*, 23–105.

——, G. Voet, A. Pacini, S. Tan, M. H. Alford, G. S. Carter, J. B. Girton, and D. Menemenlis, 2019: Pacific abyssal transport and mixing: Through the Samoan Passage versus around the Manihiki Plateau. *J. Phys. Oceanogr.*, **49**, 1577–1592, https://doi.org/10.1175/JPO-D-18-0124.1.

Reid, J. L., and P. F. Lonsdale, 1974: On the flow of water through the Samoan Passage. *J. Phys. Oceanogr.*, **4**, 58–73, https://doi.org/10.1175/1520-0485(1974)004<0058:OTFOWT>2.0.CO;2.

Roemmich, D., S. Hautala, and D. Rudnick, 1996: Northward abyssal transport through the Samoan passage and adjacent regions. *J. Geophys. Res.*, **101**, 14 039–14 055, https://doi.org/10.1029/96JC00797.

Rudnick, D. L., 1997: Direct velocity measurements in the Samoan Passage. *J. Geophys. Res.*, **102**, 3293–3302, https://doi.org/10.1029/96JC03286.

Smyth, W. D., J. N. Moum, and D. R. Caldwell, 2001: The efficiency of mixing in turbulent patches: Inferences from direct simulations and microstructure observations. *J. Phys. Oceanogr.*, **31**, 1969–1992, https://doi.org/10.1175/1520-0485(2001)031<1969:TEOMIT>2.0.CO;2.

Thomson, R. E., and W. J. Emery, 2014: *Data Analysis Methods in Physical Oceanography*. 3rd ed., Elsevier, 728 pp.

Thorpe, S. A., 1977: Turbulence and mixing in a Scottish loch. *Philos. Trans. Roy. Soc. London*, **286A**, 125–181, https://doi.org/10.1098/rsta.1977.0112.

——, J. Malarkey, G. Voet, M. H. Alford, J. B. Girton, and G. S. Carter, 2018: Application of a model of internal hydraulic jumps. *J. Fluid Mech.*, **834**, 125–148, https://doi.org/10.1017/jfm.2017.646.

Voet, G., J. B. Girton, M. H. Alford, G. S. Carter, J. M. Klymak, and J. B. Mickett, 2015: Pathways, volume transport, and mixing of abyssal water in the Samoan Passage. *J. Phys. Oceanogr.*, **45**, 562–588, https://doi.org/10.1175/JPO-D-14-0096.1.

——, M. H. Alford, J. B. Girton, G. S. Carter, J. B. Mickett, and J. M. Klymak, 2016: Warming and weakening of the abyssal flow through Samoan Passage. *J. Phys. Oceanogr.*, **46**, 2389–2401, https://doi.org/10.1175/JPO-D-16-0063.1.

Winters, K. B., and L. Armi, 2014: Topographic control of stratified flows: Upstream jets, blocking and isolating layers. *J. Fluid Mech.*, **753**, 80–103, https://doi.org/10.1017/jfm.2014.363.